

---

# **UAV Path Planning for Maximum-Information Sensing in Spatiotemporal Data Acquisition**

---

*By:*

**Andreas Nordby Vibeto**

andreanv@stud.ntnu.no

December, 2016

## **Abstract**

## **Preface**

# Contents

<b>1</b>	<b>Introduction</b>	<b>1</b>
<b>2</b>	<b>Literature Review</b>	<b>2</b>
2.1	Course controller . . . . .	2
2.1.1	Rudder as a course control surface . . . . .	2
2.1.2	Course controller with constraints . . . . .	4
2.2	Path Planner . . . . .	4
2.2.1	Path Planner for Ground Observation . . . . .	5
2.3	Hyperspectral Imaging . . . . .	6
2.3.1	Description . . . . .	6
2.3.2	UAV ground observation . . . . .	6
2.4	Summary of Literature Review . . . . .	7
<b>3</b>	<b>Kinematics</b>	<b>9</b>
3.1	UAV States . . . . .	9
3.2	Camera Position . . . . .	9
3.3	Camera Angle of View . . . . .	11
<b>4</b>	<b>Controller</b>	<b>14</b>
4.1	Dynamics . . . . .	14
4.2	Controller Transfer Function . . . . .	16
<b>5</b>	<b>Path Planner</b>	<b>18</b>
5.1	Dubins Path . . . . .	18
5.2	Altering the original path . . . . .	21
<b>6</b>	<b>Simulation</b>	<b>23</b>
6.1	Model . . . . .	23
6.2	Autopilot . . . . .	23
6.3	Path Follower . . . . .	23
<b>7</b>	<b>Simulation of Controller</b>	<b>26</b>

7.1	Controller Implementation . . . . .	26
7.2	Test Cases . . . . .	26
7.3	Results: Step Response . . . . .	27
7.4	Results: Path . . . . .	29
<b>8</b>	<b>Simulation of Path Planner</b>	<b>36</b>
8.1	Simulation Setup . . . . .	36
8.2	Result: Path Following . . . . .	37
8.3	Result: Camera Footprint . . . . .	40
8.4	Discussion . . . . .	45
<b>9</b>	<b>Conclusion</b>	<b>47</b>
9.1	Future Work . . . . .	47
	<b>References</b>	<b>48</b>

## **1 Introduction**

Unmanned Aerial Vehicles (UAV) are widely used in ground observation by equipping the UAV with different kind of sensors. While the use of UAV eases many cases of ground observation, there are some difficulties related to the attitude of the aircraft. A camera that is fixed to the UAV will be coupled with the UAVs states, so that any change in attitude will cause the camera view to shift away from the points of interest. As the height increases the error increases, so that even small attitude changes will give a difference in what is intended to be observed, and what is actually observed by the camera.

Today, it is common to attach a gimbal with a camera to the UAV to decouple the attitude of the UAV from the camera. This way the attitude of the UAV will not cause any errors in the image so that the operator can focus solely on the operation of the aircraft. However, the fuel costs of an aircraft with a gimbal attached may increase because of added weight and less effective aerodynamics.

This paper will investigate methods to reduce image errors caused by the UAVs attitude, while also avoiding the extra costs associated with gimbal. The control methods will be developed with the usage of a hyperspectral camera that is fixed to the UAV in mind. Alternative flight control methods that aim to decrease the errors caused by the coupling between the camera and the attitude of the UAV will be simulated, and their effect on the image error will be tested.

## 2 Literature Review

The literature review will be done with focus on two control methods: a controller that reduces roll during flight, and a path planner that alters the path with regards to roll and the ground points that are to be observed. The workings of hyperspectral cameras will also be reviewed, and their usage with UAVs.

### 2.1 Course controller

The course of the aircraft is normally controlled by using the ailerons to roll the aircraft, with the resulting difference between the lift vectors of each wing causing the aircraft to turn. This strategy is the most common in larger, manned aircrafts as it causes little drag and it is comfortable for the passengers [1].

Banking to change the course of the aircraft leads to problems when performing ground observation, which is solved by decoupling the roll from the sensors by using a gimbal. In order to avoid the extra payload that the gimbal is, there exists different control strategies to reduce roll during course change.

#### 2.1.1 Rudder as a course control surface

While the rudder is most commonly used to reduce the sideslip during flight, it can also be used to create sideslip which causes the aircraft to turn. The control method is a fairly common method to avoid roll during course change. KILDE HADDE VÆRT FINT. Common for these controllers is that they use the ailerons too keep the wings level during flight.

A controller using this control strategy has been created by Thomas Fisher in his paper "Rudder Augmented Trajectory Correction for Unmanned Aerial Vehicles to Decrease Lateral Image Errors of Fixed Camera Payloads" [2]. Here the term 'Rudder Augmented Trajectory Correction' (RATC) is used for a controller using the rudder to change the course, and 'Aileron Only Trajectory Correction' (AOTC) for controllers

using the ailerons as the course control surface. The implemented controller was a PD-controller simulated on a model of the Aerosonde UAV, and results focuses on image error when using a fixed camera.

The simulations showed that the course error for the two controllers were matching, both with and without wind. And unsurprisingly, the results show that the AOTC controller had much more variations in roll and the RATC controller had much more variations in sideslip. The biggest difference between the two controllers was that the RATC controller used much more input to its control surfaces, up to 400% more than the AOTC controller.

When comparing the image error for the two controllers there was a big difference in performance. The image error was measured as the distance from the camera centre point to the desired ground path, and while image errors for the RATC controller stayed at about 20 m the AOTC had a RMS error over 300 m. Field tests show the same results and prove that RATC is a good choice for reducing image erros.

A similar approach was taken by Ahsan, Rafique and Abbas in [3], but a PID controller was used instead of a PD. The controller was created from a nonlinear model which have been linearized about a stable trim point, and the resulting rudder controller was compared with a controller using the aileron for heading control.

The simulations in this paper also shows that when using rudder as a control surface the aircraft has better response compared to aileron, with less overshoot and a lower steady state error. Bode plots of the two controllers show that the rudder based course controller has a gain margin of  $-24.5dB$  and a phase margin of  $87.1^\circ$ , while the aileron based controller has a gain margin of  $-25.7dB$  and a phase margin of  $94^\circ$ . This means that the two controllers have similar stability features.

Mills, Ford and Mejias refers to a rudder-based course controller as a 'skid-to-turn' controller in [1]. They use an UAV to survey a linear infrastructure, and the desired course is calculated based on the images of the infrastructure. The control method is called Image-Based Visual Servoing (IBVS), and it creates a model of the identified structure as a straight line that the UAV will follow while ensuring the the infrastructure



stays within the camera's field of view (FOV). The controller was implemented as a PID-controller.

The controller was simulated and compared to a controller that banks the UAV to turn, and the results match the previous results: the bank-to-turn controller reduces the track error the fastest, but the skid-to-turn controller causes less error in the image plane. The controllers were also tested in wind with similar results. One thing worth noting is that when the skid-to-turn controller were to intercept the structure with tailwind it resulted in a significant overshoot. In the image plane however, the error was still smaller than for the bank-to-turn controller.

### 2.1.2 Course controller with constraints

Banking the aircraft may cause the camera's FOV to move away from the point of interest, but when controlled the aircraft can be banked without losing the point of interest. In the paper "Low Altitude Road Following Constraints Using Strap-Down EO Cameras on Miniature Air Vehicle" [4] constraints put on the UAV's roll and above ground level (AGL) ensure that the point of interest still stays within the camera's FOV when banking. In the paper the UAV tracks a roadway in a similar manner as was done in [1], and the constraints are calculated with regards to the camera's horizontal field of view, the assumed road width and the expected turn angle of the road.

The system was tested by simulating how the UAV would follow two 90° turns without wind. The results show that the road was lost from the camera's FOV two times during the two turns. This happened because the system did not estimate the road's path well enough, and the paper argues that by pointing the camera forward the estimation can be improved.

## 2.2 Path Planner

In order to successfully and efficiently execute missions using UAVs, planning is essential. Path planners are used for this reason, and there exists many different path

planners depending on the situation. A path planner may, for example, be used to avoid controlled flight into surface in mountainous areas based on maps, or it can be used in search and rescue missions to calculate in which area it is most likely to find people. In this case the path planner will be used to generate a path that will ensure that the points of interest are not lost from the camera's FOV during flight.

### 2.2.1 Path Planner for Ground Observation

Many path planners today are based on the result Dubin presented in 1957 [6]: the shortest path between two points in a two dimensional space consists of two circular arcs connected by a straight line. It has also been shown that the same principle can be used in three dimensions [7].

Dubin's path for UAVs can be used in several situations, and in [8] it is demonstrated how a Dubin's path generator can be used to search for a missing person within a given area. The path is generated by a path generator, which then transmits the path to the path-following strategy that controls the low-level autopilot. The autopilot is responsible for maintaining a constant altitude and constant airspeed, while the path generator includes a constraint to ensure it does not generate a path which requires the UAV to exceed its maximum turning rate. When the UAV finds a point of interest, a path that circulates the point is generated. The path generator is simulated, and shows that Dubin's path is a valid choice for UAV operation.

As mentioned previously in this paper, an airplane may be turned without banking by using the rudder. This strategy for airplane control can also be used in path planning, as was done by Yokoyama and Ochi [9]. A path planner based on Dubin's path was created with skid-to-turn dynamics in mind and compared with an rigorous optimization algorithm, in order to check the quasi-optimality of the Dubins's-based path. The results show that the Dubin's path algorithm always returned a feasible path that is quasi-optimal. The Dubin's path algorithm was fast, with a mean computational time of  $61.9\mu s$ , which the report concludes is fast enough for the algorithm to be used for online calculations.

## **2.3 Hyperspectral Imaging**

The control methods developed in this paper will be developed with the use of a fixed hyperspectral, pushbroom sensor in mind. A hyperspectral sensor/camera makes it possible to accurately detect types of material from the UAV, but is also sensitive to errors.

### **2.3.1 Description**

Hyperspectral imaging uses basics from spectroscopy to create images, which means that the basis for the images is the emitted or reflected light from materials [10]. The amount of light that is reflected by a material at different wavelengths is decided by several factors, and this makes it possible to distinguish different materials from each other. The reflected light is passed through a grate or a prism that splits the light into different wavelength bands, so that it can be measured by a spectrometer.

When using a hyperspectral camera for ground observation from a UAV, it is very likely that one pixel of the camera covers more than one type of material on the ground. This means that the observed wavelengths will be influenced by more than one type of material. This is called a composite or mixed spectrum [10], and the spectras of the different materials are combined additively. The combined spectra can be split into the different spectras that it is build up of by noise removal and other statistical methods which will not be covered here.

### **2.3.2 UAV ground observation**

Hyperspectral imaging is already being used for ground observation from UAVs. Its ability to distinguish materials based on spectral properties means that it can be used to retrieve information that normal cameras are not able to. For example in agriculture it can be used to map damage to trees caused by bark beetles [11], or it can be used to measure environmental properties, for example chlorophyll fluorescence, on leaf-level in a citrus orchard [12].

Systems for ground observation with hyperspectral cameras can be very complex, which often leads to heavy systems. In [13], a lightweight hyperspectral mapping system was created for the use with octocopters. The purpose of the system is to map agricultural areas using a spectrometer and a photogrammetric camera, and the final "ready-to-fly" weight of the system is 2.0 kg. The resolution of the final images made it possible to gather information on a single-plant basis, and the georeferencing accuracy was off by only a few pixels.

The tests were done at a low altitude, maximum 120 m. While this was mainly because of local regulations, it also gave a benefit as there was less atmosphere disturbance in the measurements. The UAVs orientation data combined with surface models was used when recovering the positional data in the images. However, they found that externally produced surface models was not accurate enough as they do not take vegetation into consideration. For this reason they supplemented the existing surface models with information gathered during flight.

## 2.4 Summary of Literature Review

The literature review shows that the problem viewed here have already been addressed, and that there already exists control methods that seeks to minimize image error. The review also shows that hyperspectral pushbroom cameras are being used for ground observation today and that these systems are moving from being large and heavy, to being reduced to a size more fitting for UAVs.

One additional point made in [2] that is worth noting is that the RATC controller will ease the flight plans for ground observing. When using AOTC controllers for ground observing, extra measures often have to be taken to ensure that the entire area of interest is covered by the camera. For a typical  $90^\circ$  turn this could be to fly past the turn, make complete circle in the opposite direction of the turn, and then continue on the path after the  $90^\circ$  bend. When using the RATC controller developed, the flight path length and time was reduced by about 80%, and it was estimated that the reduction in length and time will give a 75% reduction in energy usage. This means that even though the paper

concluded the RATC used 400% more input than the AOTC, the RATC will save time and maybe energy for complicated paths with many turns.

### 3 Kinematics

#### 3.1 UAV States

In order to control the UAV with regards to where the camera is pointing, a kinematic model that maps the camera focus to the UAV position and attitude is needed. The position of the UAV will be given in reference frame  $\{n\}$  using the North East Down (NED) coordinate frame:

$$\mathbf{p}_{b/n}^n = \begin{bmatrix} N \\ E \\ D \end{bmatrix} = \begin{bmatrix} x_n \\ y_n \\ z_n \end{bmatrix} \quad (3.1)$$

The attitude of the UAV will be given as Euler-angles:

$$\boldsymbol{\Theta}_{nb} = \begin{bmatrix} \phi \\ \theta \\ \psi \end{bmatrix} \quad (3.2)$$

where  $\phi$  represents the roll angle,  $\theta$  the pitch angle and  $\psi$  the heading angle. The attitude angles have the corresponding angular velocities noted  $p$ ,  $q$  and  $r$  respectively. In all the simulations done in this paper there will be no wind, and therefore it can be assumed that the course angle  $\chi$  is equal to the heading  $\psi$ .

#### 3.2 Camera Position

The position of the camera center point is coupled with the attitude of the aircraft. Figure 1 shows how the position of the camera is affected by the attitude  $\boldsymbol{\Theta}_{nb}$  in the body frame  $\{b\}$ , and the height  $z_n$  in the NED frame  $\{n\}$ . This model assumes flat earth. The camera position in the body frame  $\{b\}$  is expressed as

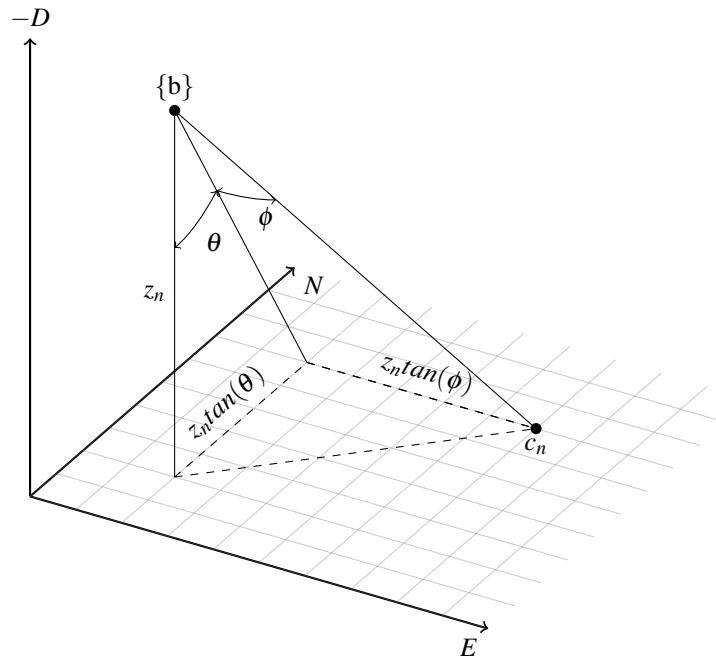


Figure 1: Illustration of how the aircraft attitude influence the camera position.

$$\mathbf{c}_b^b = \begin{bmatrix} c_{x/b}^b \\ c_{y/b}^b \end{bmatrix} = \begin{bmatrix} z_n \tan(\theta) \\ z_n \tan(\phi) \end{bmatrix}. \quad (3.3)$$

In order to express the camera position  $\mathbf{c}_b^b$  in  $\{n\}$ , the heading  $\psi$  of the aircraft must be taken into consideration. This is done by rotating the point  $\mathbf{c}_b^b$  with the rotational matrix  $\mathbf{R}_{z,\psi}$ :

$$\mathbf{c}_b^n = \begin{bmatrix} c_{x/b}^n \\ c_{y/b}^n \end{bmatrix} = \mathbf{R}_{z,\psi} \mathbf{c}_b^b, \quad (3.4)$$

where:

$$\mathbf{R}_{z,\psi} = \begin{bmatrix} \cos(\psi) & -\sin(\psi) & 0 \\ \sin(\psi) & \cos(\psi) & 0 \\ 0 & 0 & 1 \end{bmatrix}. \quad (3.5)$$

The point  $\mathbf{c}_b^n$  is not the actual position in  $\{n\}$  since it does not take the UAVs position into consideration. This is done by simply adding the UAVs position to  $\mathbf{c}_b^n$ :

$$\mathbf{c}^n = \begin{bmatrix} c_x^n \\ c_y^n \end{bmatrix} = \begin{bmatrix} x_n + c_{x/b}^n \\ y_n + c_{y/b}^n \end{bmatrix}. \quad (3.6)$$

### 3.3 Camera Angle of View

Since the camera isn't only focusing on one specific point, it can be useful describing the camera footprint of a pushbroom sensor as two extremities instead of one center point. Equation (3.3) can easily be changed to do this. Assuming the camera has an angle of view  $\sigma$ , the equation now becomes:

$$\mathbf{e}_{1,b}^b = \begin{bmatrix} e_{x/b}^b \\ e_{y_{1/b}}^b \end{bmatrix} = \begin{bmatrix} z_n \tan(\theta) \\ z_n \tan(\phi + \sigma) \end{bmatrix}, \quad \mathbf{e}_{2,b}^b = \begin{bmatrix} e_{x/b}^b \\ e_{y_{2/b}}^b \end{bmatrix} = \begin{bmatrix} z_n \tan(\theta) \\ z_n \tan(\phi - \sigma) \end{bmatrix}. \quad (3.7)$$



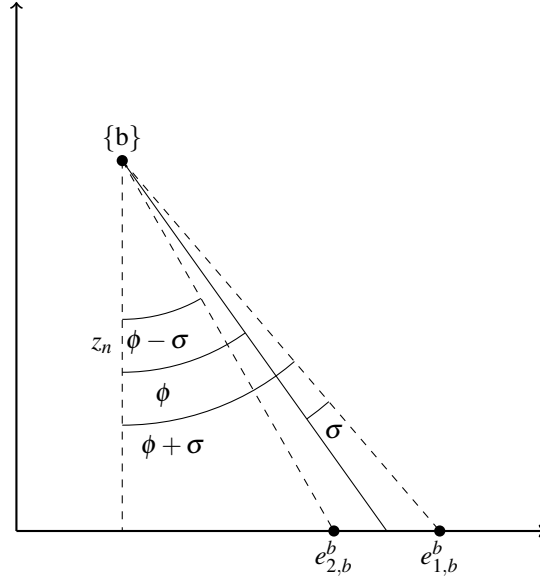


Figure 2: Illustration of how the field of view for a pushbroom sensor is calculated.

The steps for translating the points to the NED frame are the same as in (3.4) and (3.6):

$$\mathbf{e}_b^n = \begin{bmatrix} e_{x/b}^n \\ e_{y/b}^n \end{bmatrix} = \mathbf{R}_{z,\psi} \mathbf{e}_b^b \quad (3.8)$$

$$\mathbf{e}^n = \begin{bmatrix} e_x^n \\ e_y^n \end{bmatrix} = \begin{bmatrix} x_n + e_{x/b}^n \\ y_n + e_{y/b}^n \end{bmatrix}. \quad (3.9)$$

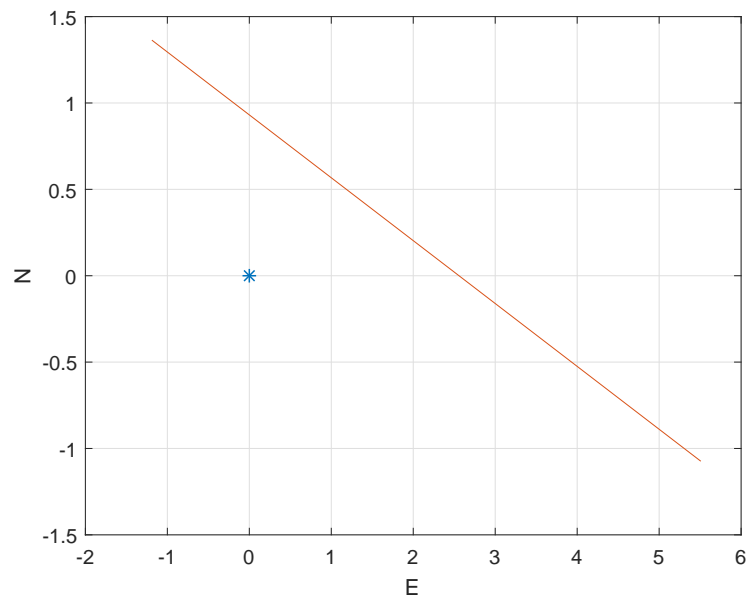


Figure 3: Graph showing the line the camera captures when the plane is positioned in the origin with an altitude of  $10m$ , and  $\phi = -10$ ,  $\theta = -5$  and  $\psi = 20$ . The field of view is  $20^\circ$ .

## 4 Controller

### 4.1 Dynamics

In his paper, Fisher [2] uses the dynamic model given in Beard and McLain [5] to develop a controller that uses rudder to change the heading. A similar controller will be used in this paper, and it will be derived by using the same method as Fisher used.

To simplify the controller, it will be assumed that there is no wind and no sideslip  $\beta$ . These assumption will simplify the control problem since it can be assumed that  $\chi = \psi$ . It will also be assumed that the UAV is in trimmed, straight level flight, as this will simplify the system since the roll angle  $\phi$  and pitch angle  $\theta$  both can be assumed to be small.

The yaw dynamics for a UAV are (eq. 3.17, Beard and McLain [5])

$$\dot{r} = \Gamma_7 pq - \Gamma_1 qr + \Gamma_4 l + \Gamma_8 n \quad (4.1)$$

where  $l$  and  $n$  are the moments about the  $\mathbf{i}^b$  and  $\mathbf{j}^b$  axes respectively. The  $\Gamma$  equations describe the inertia of the aircraft and are expressed using elements of the inertia matrix  $\mathbf{J}$ .

The heading dynamic is expressed by the pitch rate  $q$ , the yaw rate  $r$ , and the attitude states  $\Theta_{nb}$  (eq. 3.3, Beard and McLain [5]):

$$\dot{\psi} = \sin(\phi)\sec(\theta)q + \cos(\phi)\sec(\theta)r. \quad (4.2)$$

As mentioned it is assumed that the aircraft is in trimmed straight level flight. By assuming small  $\phi$  and  $\theta$ , and also no pitch rate  $q$ , the heading dynamics can be simplified to:

$$\dot{\psi} = r, \quad (4.3)$$

which leads to:

$$\ddot{\psi} = \dot{r}. \quad (4.4)$$

The equation for the yaw dynamics (4.1) can now be written as

$$\ddot{\psi} = \dot{r} = \Gamma_4 l + \Gamma_8 n. \quad (4.5)$$

The moments  $l$  and  $n$  are the moments on the aircraft caused by the attitude states and rates, the sideslip  $\beta$ , and also the aileron deflection  $\delta_a$  and the rudder deflection  $\delta_r$ .

These are given by equation 4.15 and 4.16 in Beard and McLain [5]:

$$l = \frac{1}{2} \rho V_a^2 S b [C_{l_0} + C_{l_\beta} \beta + C_{l_p} \frac{b}{2V_a} p + C_{l_r} \frac{b}{2V_a} r + C_{l_{\delta_a}} \delta_a + C_{l_{\delta_r}} \delta_r] \quad (4.6a)$$

$$n = \frac{1}{2} \rho V_a^2 S b [C_{n_0} + C_{n_\beta} \beta + C_{n_p} \frac{b}{2V_a} p + C_{n_r} \frac{b}{2V_a} r + C_{n_{\delta_a}} \delta_a + C_{n_{\delta_r}} \delta_r]. \quad (4.6b)$$

By continuing to follow Fishers [2] notation, equations (4.5) and (4.6a) can be combined to get

$$\ddot{\psi} = \frac{1}{2} V_a^2 S b [C_{r_0} + C_{r_\beta} \beta + C_{r_p} \frac{b}{2V_a} p + C_{r_r} \frac{b}{2V_a} r + C_{r_{\delta_a}} \delta_a + C_{r_{\delta_r}} \delta_r] \quad (4.7)$$

where

$$C_{r_0} = \Gamma_4 C_{l_0} + \Gamma_8 C_{n_0} \quad (4.8a)$$

$$C_{r_\beta} = \Gamma_4 C_{l_\beta} + \Gamma_8 C_{n_\beta} \quad (4.8b)$$

$$C_{r_p} = \Gamma_4 C_{l_p} + \Gamma_8 C_{n_p} \quad (4.8c)$$

$$C_{r_r} = \Gamma_4 C_{l_r} + \Gamma_8 C_{n_r} \quad (4.8d)$$

$$C_{r_{\delta_a}} = \Gamma_4 C_{l_{\delta_a}} + \Gamma_8 C_{n_{\delta_a}} \quad (4.8e)$$

$$C_{r_{\delta_r}} = \Gamma_4 C_{l_{\delta_r}} + \Gamma_8 C_{n_{\delta_r}} \quad (4.8f)$$

where the constants are craft-specific parameters, and

$$\Gamma_4 = \frac{J_{xz}}{J_x J_z - J_{xz}^2} \quad (4.9a)$$

$$\Gamma_8 = \frac{J_x}{J_x J_z - J_{xz}^2}. \quad (4.9b)$$

## 4.2 Controller Transfer Function

Since the controller is to use rudder input  $\delta_r$  to change the heading  $\psi$ , equation (4.7) can be rearranged to express these variables:

$$\ddot{\psi} = -a_{\psi_1} \dot{\psi} + a_{\psi_2} \delta_r + d_{\psi} \quad (4.10)$$

where

$$a_{\psi_1} = -\frac{1}{4} \rho V_a S b^2 C_{r_r} \quad (4.11a)$$

$$a_{\psi_2} = \frac{1}{2} \rho V_a^2 S b^2 C_{r_{\delta_r}} \quad (4.11b)$$

$$d_{\psi} = \frac{1}{2} \rho V_a^2 S b [C_{r_0} + C_{r_{\beta}} \beta + C_{r_p} \frac{b}{2V_a} p + C_{r_{\delta_a}} \delta_a]. \quad (4.11c)$$

$a_{\psi_1}$  is chosen to be negative as this will ease later calculations (see (4.17a)). The Laplace transformation brings (4.10) to the form

$$\psi(s) = \frac{a_{\psi_2}}{s(s + a_{\psi_1})} \delta_r(s) + \frac{1}{s(s + a_{\psi_1})} d_{\psi}(s). \quad (4.12)$$

This equation show that the second term containing  $d_{\psi}$  acts as a disturbance for the controller. As shown in (4.11c), the inputs to this term are the sideslip  $\beta$ , roll rate  $p$ , and aileron deflection  $\delta_a$ . Since the UAV is assumed to be in trimmed straight level flight and the controller will use the rudder to turn instead of roll it is already assumed that  $p$  will be zero, as will the aileron deflection  $\delta_a$ . During normal operation it cannot be assumed that no sideslip will occur. However, any  $\beta$  is assumed to be small so

that it can be removed from the controller equation. The final transfer function for the controller dynamics will then be

$$\frac{\psi(s)}{\delta_r(s)} = \frac{a_{\psi_2}}{s(s + a_{\psi_1})}. \quad (4.13)$$

In order to control the heading of the UAV with the help of the rudder, a controller must be added. The PD controller used here takes the form

$$\delta_r = ek_p + \dot{e}k_d \quad (4.14)$$

where  $e$  is defined as the error between the desired heading  $\psi_d$  and the measured heading  $\psi$

$$e = \psi_d - \psi. \quad (4.15)$$

The transfer function between the desired heading and the measured heading is found by adding the controller to the transfer function between rudder and heading (4.13)

$$\frac{\psi}{\psi_d} = \frac{a_{\psi_2}k_p}{s^2 + (a_{\psi_1} + a_{\psi_2}k_d)s + a_{\psi_2}k_p}. \quad (4.16)$$

Since the transfer function is written in the form of a canonical second-order transfer function, the proportional gain  $k_p$  and the derivative gain  $k_d$  can be found by calculating the natural frequency  $\omega_n$  and damping factor  $\zeta$ . The final expressions for the gains will be

$$k_p = \frac{\omega_n^2}{a_{\psi_2}} \quad (4.17a)$$

$$k_d = \frac{2\zeta\omega_n - a_{\psi_1}}{a_{\psi_2}}. \quad (4.17b)$$

## 5 Path Planner

In an attempt to better track the ground path with regards to the camera, a simple path planner will be developed. The goal of the path planner is to alter the position of the aircraft so that the camera will be focused on the point of interest on the ground, regardless of the attitude of the aircraft. The path will first be generated as a Dubins path that later will be altered with regards to the kinematic model developed in chapter 3.

### 5.1 Dubins Path

As already presented in chapter 2.2.1, a Dubin's path consists of two circular arcs connected by a straight line [6]. The path generated here will only be in two dimensions, as it is assumed that the aircraft's autopilot will maintain a constant height. In order for a vehicle to follow a Dubins path, it must be possible to describe the kinematics of the vehicle as a Dubins vehicle [14]:

$$\dot{x}(t) = \cos(\theta(t))u_1(t) \quad (5.1a)$$

$$\dot{y}(t) = \sin(\theta(t))u_1(t) \quad (5.1b)$$

$$\dot{\theta}(t) = u_2(t) \quad (5.1c)$$

where  $u_1$  is the linear velocity,  $u_2$  is the angular velocity and  $\theta$  is the heading angle. For the kinematic model of the aircraft in this paper,  $u_1$  equals to  $V$ ,  $\theta$  equals to  $\psi$ , and  $u_2$  equals to  $r$ .

When generating a Dubins path there are four cases that need to be taken into consideration [5]. Depending on the start and end configuration a Dubins path can either start and end with a circle that the vehicle traces either clockwise or counterclockwise, and the four cases are the different combinations of start and end circle.

In order to generate a Dubins path for this paper the algorithm proposed in Beard & McLain was used (algorithm 7, [5]). The algorithm takes the start and end position,

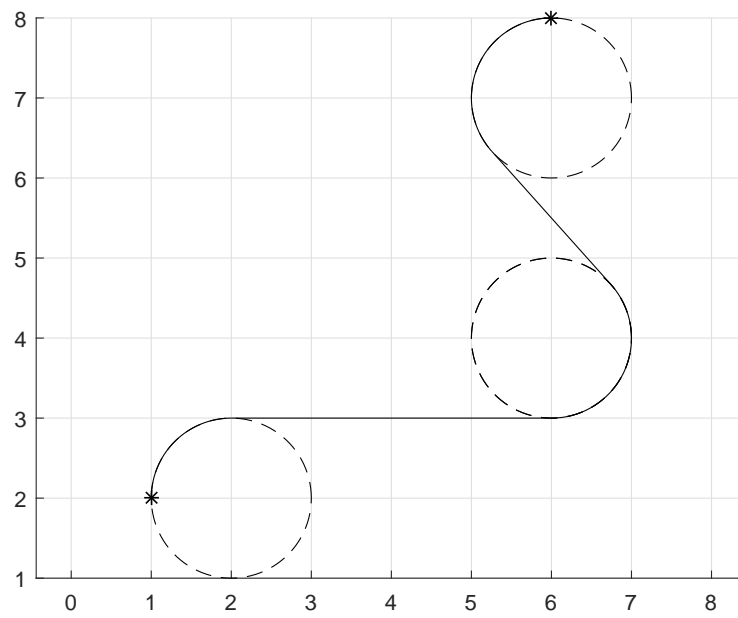


Figure 4: Illustration of a simple Dubins path.



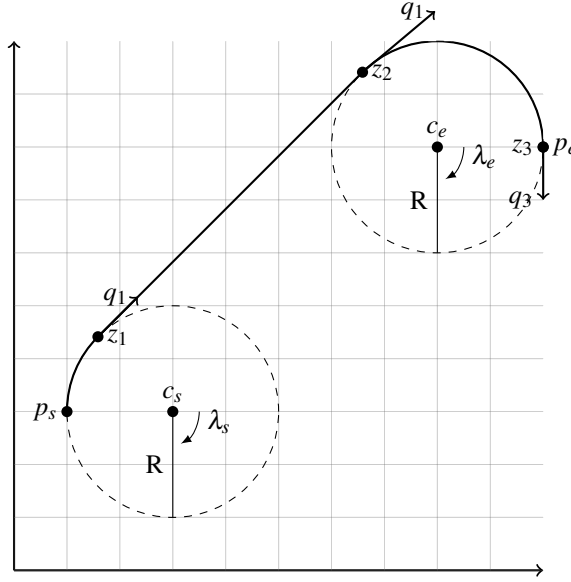


Figure 5: Illustration of the parameters returned by the Dubins algorithm.

start and end heading and radius of the circles as input. Based on these parameters the algorithm calculates the length of the path created by any of the four cases, and the case that gives the shortest path length is chosen. The outputs of the algorithm is the length of the path together with other parameters describing the path. The parameters that are calculated by the algorithm are shown in 5.

The algorithm that generates the Dubins path only generates the path between two points, hence another algorithm is needed in order to generate the Dubins path involving several waypoints. For this another algorithm by Beard & McLain (algorithm 8, [5]) was used. This algorithm takes a list of waypoints together with the position of the aircraft and the desired turning radius as input. Based on the inputs the algorithm generates a Dubins path and then calculates where on the path the aircraft is. It returns information about whether or not the aircraft should follow a straight line or track a circle, and the information needed to do this. This information is given to two algorithms that calculate the desired heading that can be fed to the autopilot. These algorithms will be described in chapter 6.3.

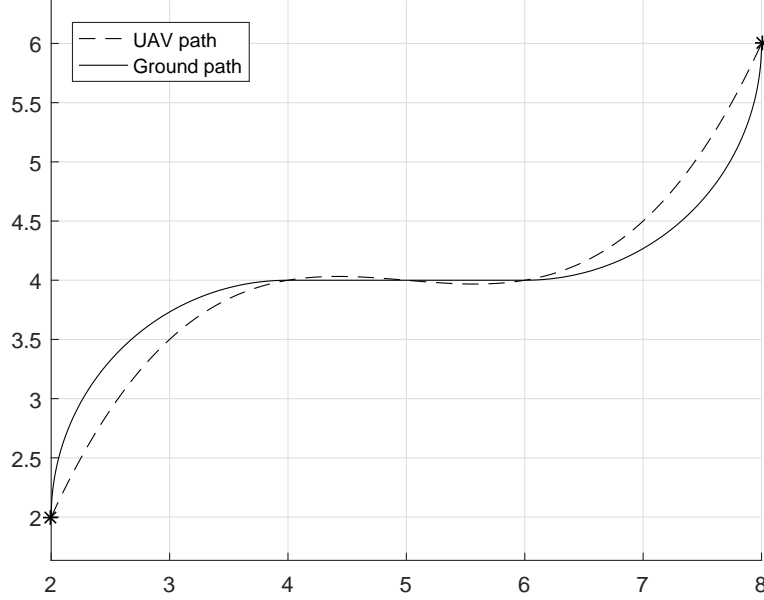


Figure 6: Illustration of the principle for altering the path.

## 5.2 Altering the original path

The Dubins path described in the previous section will be used to generate a path based on the initial waypoints that the UAV is to observe. The problem with this path is that it will tell the aircraft to turn when it is just above the ground path, and the roll used to turn will cause the fixed camera to lose the points of interest from its field of view.

In order to compensate for the roll of the aircraft, the Dubins path will be altered so that the camera is always pointing at the points of interest. The principle is shown in figure 6.

In order to compensate the roll the kinematic model developed in 3 can be used. For altering the path only the distance from the aircraft frame  $\{b\}$  to the camera point caused by the roll is needed. This corresponds to  $c_{y/b}^b$  from equation (3.3):

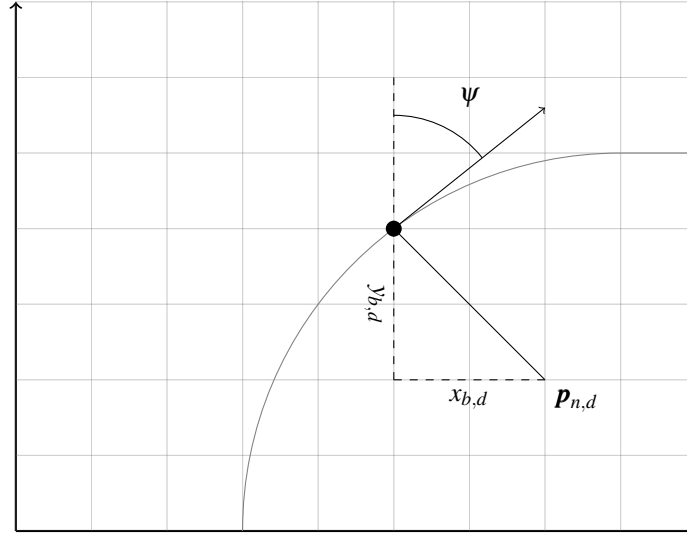


Figure 7: Illustration of the direction for altering the path.

$$c_{y/b}^b = z_n \tan(\phi). \quad (5.2)$$

$c_{y/b}^b$  only represents the distance the path is to be moved, and not the direction. The direction the path is to be moved is given by the heading  $\psi$ , and the direction should be perpendicular to  $\psi$  as shown in figure 7. The coordinates for the new path  $p_d$  in the body frame  $\{b\}$  then becomes

$$p_{b,d} = \begin{bmatrix} x_{b,d} \\ y_{b,d} \end{bmatrix} = \begin{bmatrix} c_{y/b}^b \sin(\psi) \\ -c_{y/b}^b \cos(\psi) \end{bmatrix}, \quad (5.3)$$

and in the NED frame  $\{n\}$ :

$$p_{n,d} = p_{b/n}^n + p_{b,d}. \quad (5.4)$$

## 6 Simulation

The simulations of the controller will be performed using Matlab, with a model of the Aerosonde UAV.

### 6.1 Model

The model of the Aerosonde UAV is based on parameters and equations given by Beard & McLain [5]. The model was implemented by Gryte as a part of his master thesis [15].

The model is split into two parts, forces and aircraft dynamics. The forces module implements the equations for describing all the forces working on the aircraft, based on wind, aircraft states and the control inputs. The calculated forces are then sent to the aircraft dynamics module which calculates the new states of the aircraft based on the forces.

### 6.2 Autopilot

The autopilot used in the simulations have also been implemented by Gryte [15], and it is based on equations in Beard & McLain [5] as well. The autopilot have previously been used with a different UAV, and therefore needed to be tuned in order to control the Aerosonde UAV. The controller loops are defined by relative damping factor  $\zeta$  and natural frequency  $\omega_n$ , and by implementing the control loops outside the model the parameters can be found separately. This makes a good starting point for further tuning.

### 6.3 Path Follower

Three different path followers will be used in this simulation. One of the three path followers will be used to navigate between waypoints by the rudder controller, while the other two will be used to follow the paths generated by the path planner.

The strategy used to follow Dubins path will be based on two algorithms presented in [5] by Beard & McLain. The two algorithms are used to follow straight and curved line paths.

In order to follow straight line paths, the algorithm uses the position and heading of the aircraft, the previous waypoint and the direction from the previous to the next waypoint as input. The previous waypoint and direction to the next waypoint are given as output from the algorithm generating Dubins path described in chapter 5.1. The new course is calculated so that the aircrafts position will converge towards the original path.

The algorithm for following circular paths is based on following perfect circles. Therefore it takes center and radius of the circle, the direction to orbit the circle, and the current position and heading of the aircraft. The heading calculated here will also ensure that the aircrafts position converges to the circular path.

The altered path is based on the route that is flown in the first simulation, and will therefore not consist of circular arcs and straight lines. Instead the path will be a continuous path which requires a different path follower. The path follower will be based on the principles of Line Of Sight (LOS) steering laws presented by Fossen [19].

Enclosure-based steering is LOS principle that considers a circle with radius  $R$  enclosing the vehicle, which represents the LOS distance. Assuming that the radius is sufficiently large compared to the vehicle's distance from the path, the circle will intersect the path at two different points. One of the points will be in the direction of the vehicle, denoted  $x_{los}$  and  $y_{los}$ . This is the point the vehicle will be directed to, and the course to that point can be expressed as [19]:

$$\chi_d(t) = \text{atan2}(y_{los} - y(t), x_{los} - x(t)) \quad (6.1)$$

where  $x(t)$  and  $y(t)$  is the vehicle's current position. Using Pythagoras theorem, the points  $x_{los}$  and  $y_{los}$  can be found as:

$$[x_{los} - x(t)]^2 + [y_{los} - y(t)]^2 = R^2 \quad (6.2)$$

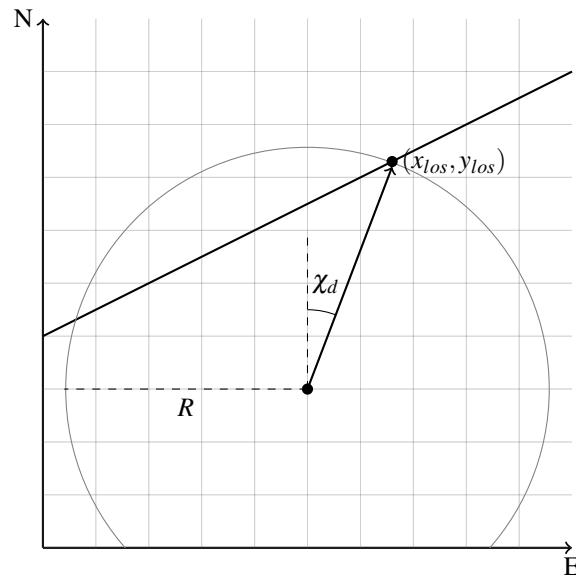


Figure 8: Illustration of enclosed line-of-sight path following.

where  $R$  is the chosen LOS distance.

## 7 Simulation of Controller

For the simulation the controller was implemented in Simulink, and it operates alongside the autopilot described in chapter 6. Since the controller will be used to control course using the rudder, the autopilot will be controlling all the other states and actuators.

### 7.1 Controller Implementation

The controller was implemented using a simple block diagram in Simulink, with desired course as input and rudder control as output. As a starting point for the controller tuning the control loop was simulated in an open loop.

### 7.2 Test Cases

The altitude used when using a pushbroom sensor from an UAV for ground observation varies with what is being observed and the equipment used. When observing the vegetation, low-altitudes around 100 m is often used ([13], [16], [17]). However, altitudes as high as 1900 m has also been used to observe agricultural crops ([18]). In this paper simulations will be performed mainly at 100 m. The FOV for the camera will be set to  $19^\circ$  (approximately the same as in [13]).

The controller has been tested in two different cases. The first case is a simple  $45^\circ$  turn in order to test the step response of the controller, and the response will be compared with a controller using ailerons to turn. In the second case the UAV will follow a ground path that is to be observed, and a comparison of the camera footprint made by the two controllers will be performed.

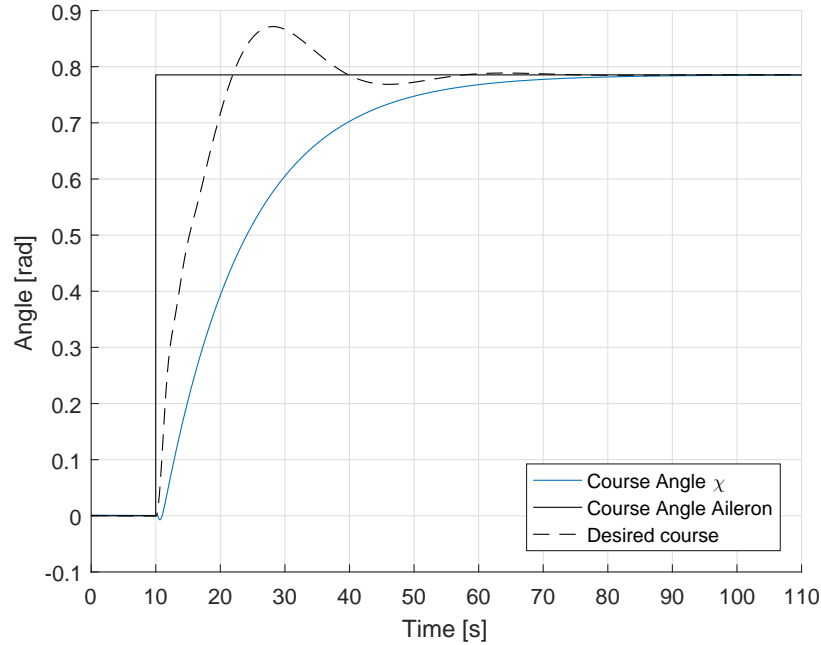


Figure 9: The step response of the course controller, compared to the course step response of a course controller using the ailerons.

### 7.3 Results: Step Response

The step response of the controller is shown in figure 9, together with the step response of a controller using the aileron to turn. The course angle  $\chi$  reaches the desired  $45^\circ$  ( $0.76 \text{ rad}$ ) after about 80 seconds. This is 20 seconds after the aileron-controller starts to stabilize at  $45^\circ$ , and while the aileron-controller is underdamped the rudder-controller is overdamped. Just after the step response has occurred, the course angle for the rudder-controller starts off in the slightly wrong direction before it starts increasing.

Figure 10 show that the pitch  $\theta$  has only small variations when the step response occurs. When the step occurs the roll  $\psi$  changes rapidly back and forth. This is because the deflection of the rudder actuator also induces a roll on the aircraft. This can also be seen on the inputs shown in figure 11. At the time of the step both the aileron and the



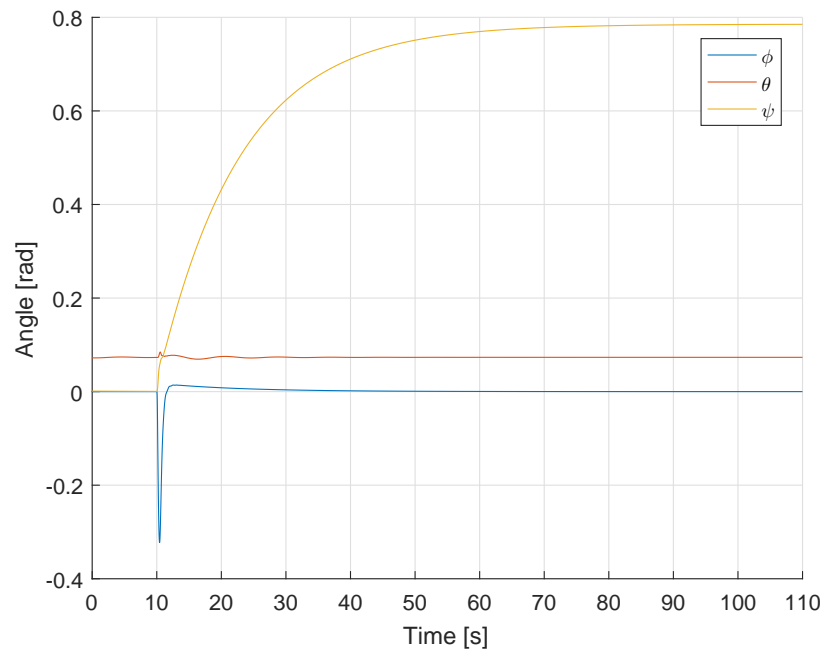


Figure 10: The attitude states of the UAV during the step response.

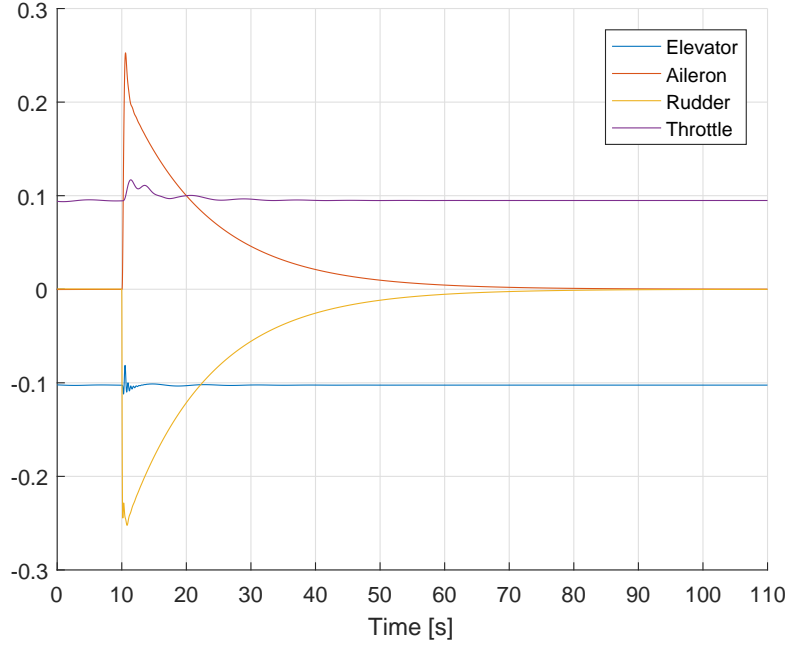


Figure 11: Input used during the step response. The input is given as a signal between  $\pm 1$ .

rudder increases rapidly, with an almost "mirrored" response.

The bode-plot in figure 12 shows the frequency response of the rudder controller. The phase margin is  $61.2^\circ$  and since the phase never goes below  $-180^\circ$ , this is a stable system (ch. 8.4.7, [20]). This tuning was achieved with  $\zeta$  set to 0.6 and  $\omega_n$  set to 3.5, which corresponds to a  $k_p$  of  $-0.3574$  and a  $k_d$  of 0.2090.

## 7.4 Results: Path

The results of the simulation for the rudder controller can be seen in figures 13 and 14. The figures show that the controller manages to keep the ground path that is to be observed within the camera footprint when the path is straight. However, it does need to be a sharp turn for the camera to shift away from the ground path. The effect of the

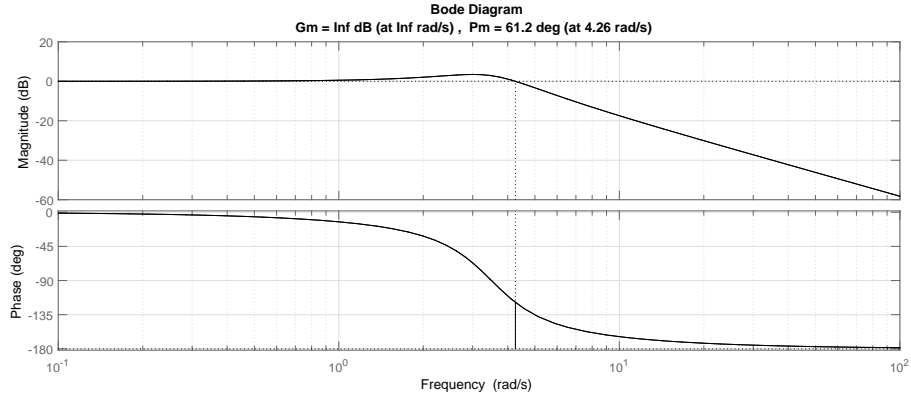


Figure 12: The camera footprint during simulation of the first path.

roll that the rudder induces, which can be seen in figure 10 with the step response, is also visible on the camera footprint. At the beginning of each turn there are a small "NUDGE" in the footprint, but none of them moves the camera outside the observation path.

The flown path and the camera footprint for the controller using the aileron to change course is shown in figures 15 and 16. The observation path is within the camera footprint almost throughout the flight, but the edge of the camera footprint is close to the observation path at multiple times. At the beginning of every turn there is rapid shift in the camera footprint because of an abrupt roll change, and after every turn the roll of the aircraft is swining back and forth before it settles.

The camera footprint for the two paths are shown in figure 17. The figure shows that the camera footprint of the aileron controller SWINGS more than the footprint of the rudder controller, but it doesn't necessarily move further away from the observation path. At the beginning of the turns both of the controllers causes a "NUDGE" in the camera footprint in opposite directions. The "NUDGE" of the aileron controller is bigger and remains longer than the "NUDGE" for the rudder controller.

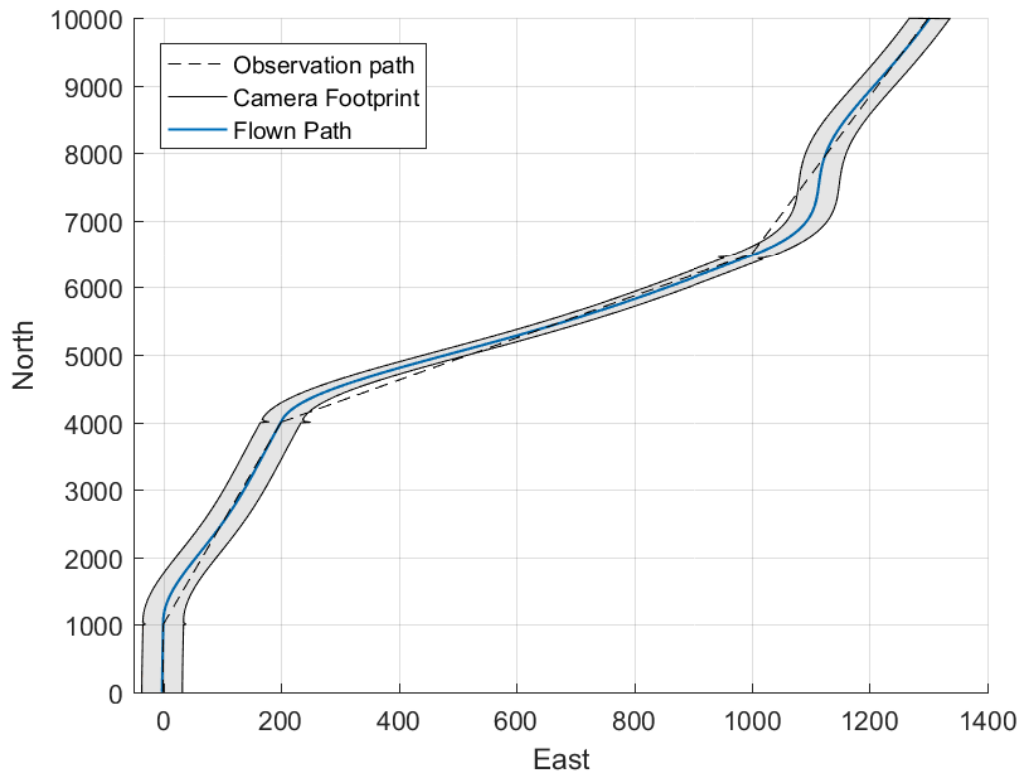


Figure 13: The path flown and the camera footprint when following the path using the rudder controller. Altitude is 100 m.

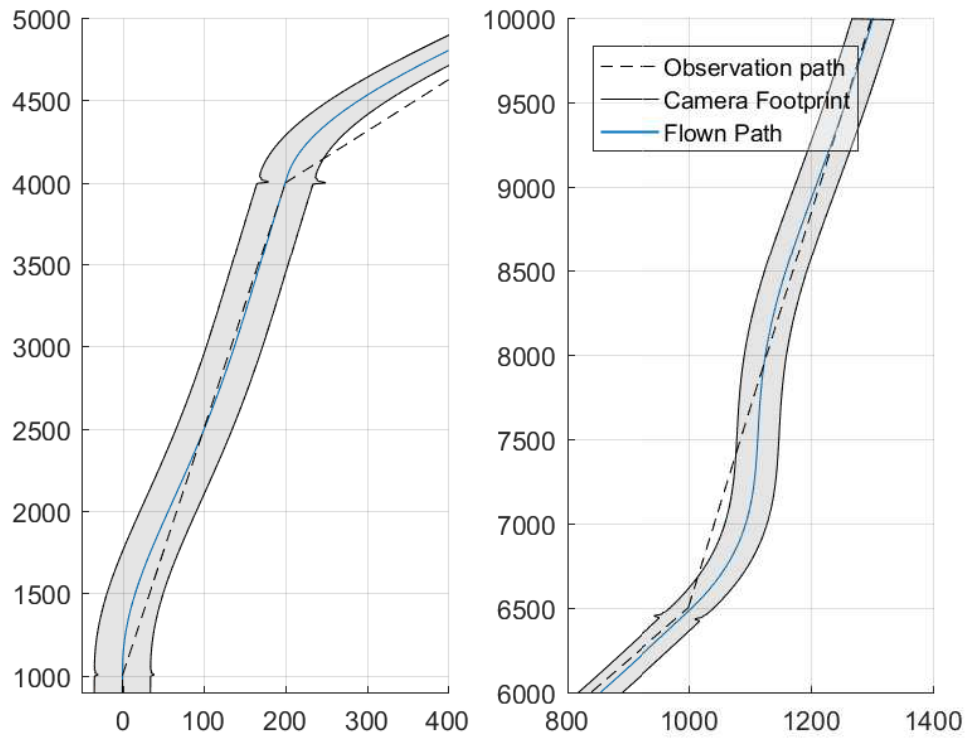


Figure 14: Detailed view of the path flown and the camera footprint when following the path using the rudder controller. Altitude is 100 m.

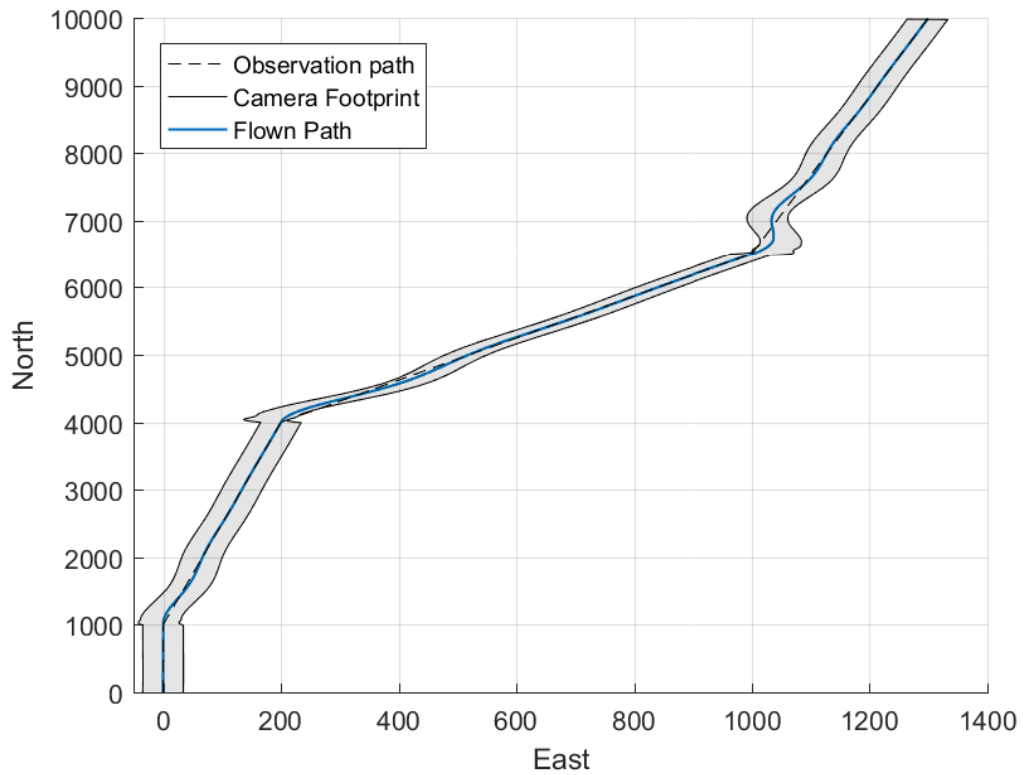


Figure 15: The path flown and the camera footprint when following the path using the aileron controller. Altitude is 100 m.

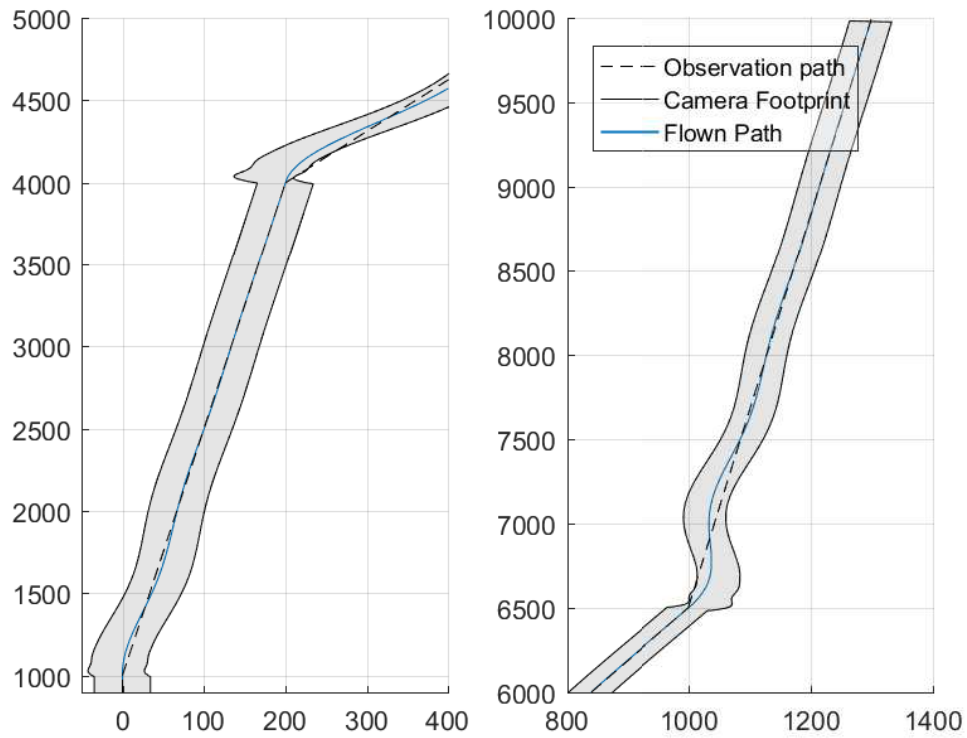


Figure 16: Detailed view of the path flown and the camera footprint when following the path using the aileron controller. Altitude is 100 m.

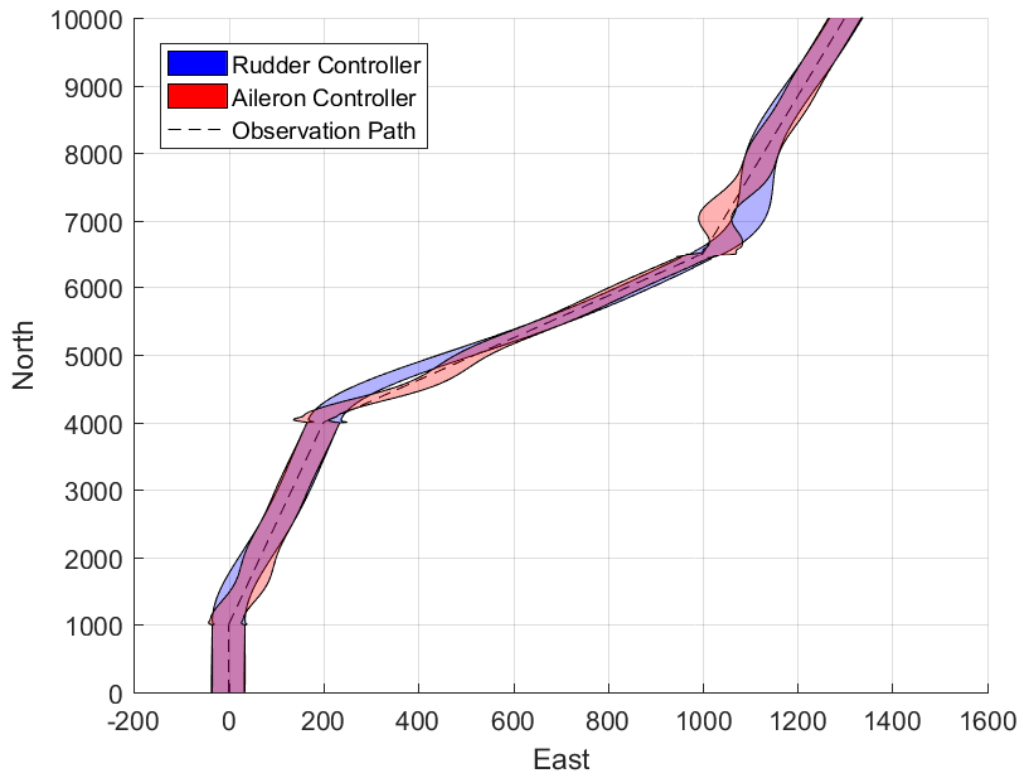


Figure 17: A comparison of the camera footprints of the two controllers. Altitude is 100 m.



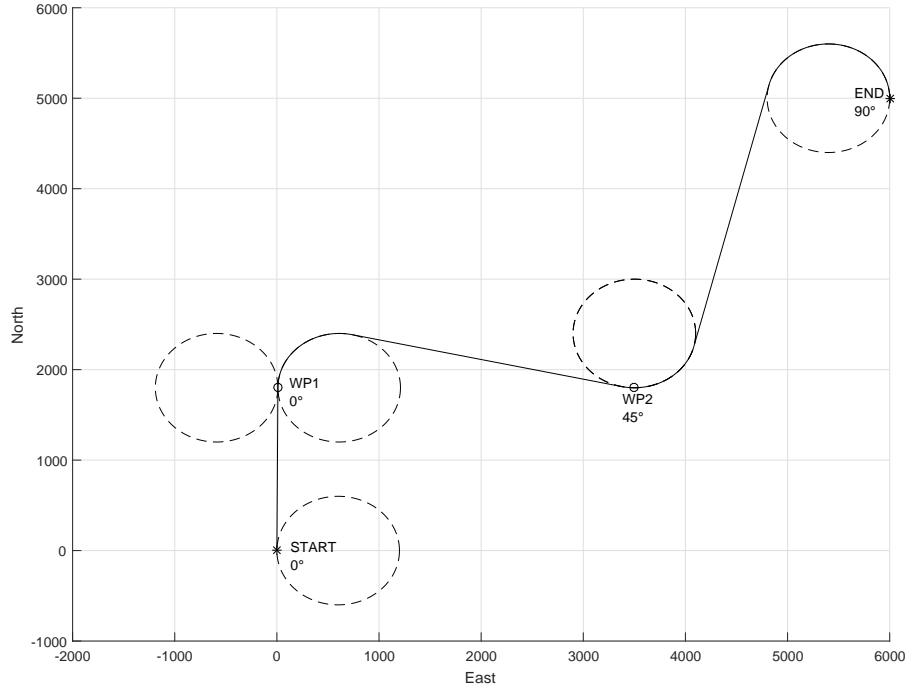


Figure 18: The path that will be simulated, with the direction associated with every waypoint.

## 8 Simulation of Path Planner

The same autopilot that was used for simulating the controller will be used when simulating the path planner. A path follower will be used to give course commands to the autopilot during simulation, while the rest of the states will be controlled only by the autopilot.

### 8.1 Simulation Setup

The simulation was performed using the same Simulink and Matlab setup as previously, using the path followers to generate the desired course angle. The Dubin's path that will be used as a reference is shown in figure 18.

The radius of the circles in the Dubins path was chosen to 600 m, and is the same for every waypoint. If it is assumed that there is no wind and no sideslip, the equation for a coordinated turn becomes [5]:

$$R = \frac{V_g^2}{g \tan(\phi)}. \quad (8.1)$$

With  $R$  set to 600 m, and the airspeed equal to the groundspeed at 35 m/s, the corresponding roll  $\phi$  is about  $15^\circ$ . This seems reasonable, as it is not expected that a UAV performing ground observation will be performing high dynamic manoeuvres. The LOS distance was set to 200 m by trial and failure.

## 8.2 Result: Path Following

Figure 19 and figure 20 shows the result of the simulation when the UAV follows the generated Dubins path that is to be observed. The aircraft follows the observation path closely, and in turns it drifts slightly off and takes the outer turn.

Figure 21 shows the attitude states of the aircraft during the flight, and shows that the roll  $\phi$  is just below 0.25 rad for each turn, which is about  $15^\circ$  as predicted previously. However, it can be seen that  $\phi$  varies during the course changes, meaning that the aircraft is not doing a perfectly smooth turn. When using equation (5.2) to calculate how the path should be altered, these uneven turns will cause the path to be uneven as well. The altered path is shown together with the original flown path in figure 22. The figure shows some "NUDGES" due to the uneven turn, mainly at the beginning and end of the turns.

The altered path is supposed to counteract the slow and more constant changes in roll during a turn. The changes in roll caused by the uneven turn are much faster than the slow changes. This means that the unwanted changes in roll can be removed by passing the signal through a low-pass filter. The result of altering the path with the low-pass filtered  $\phi$  is shown in figure 23, and the result that the new path is smoother than the first one.

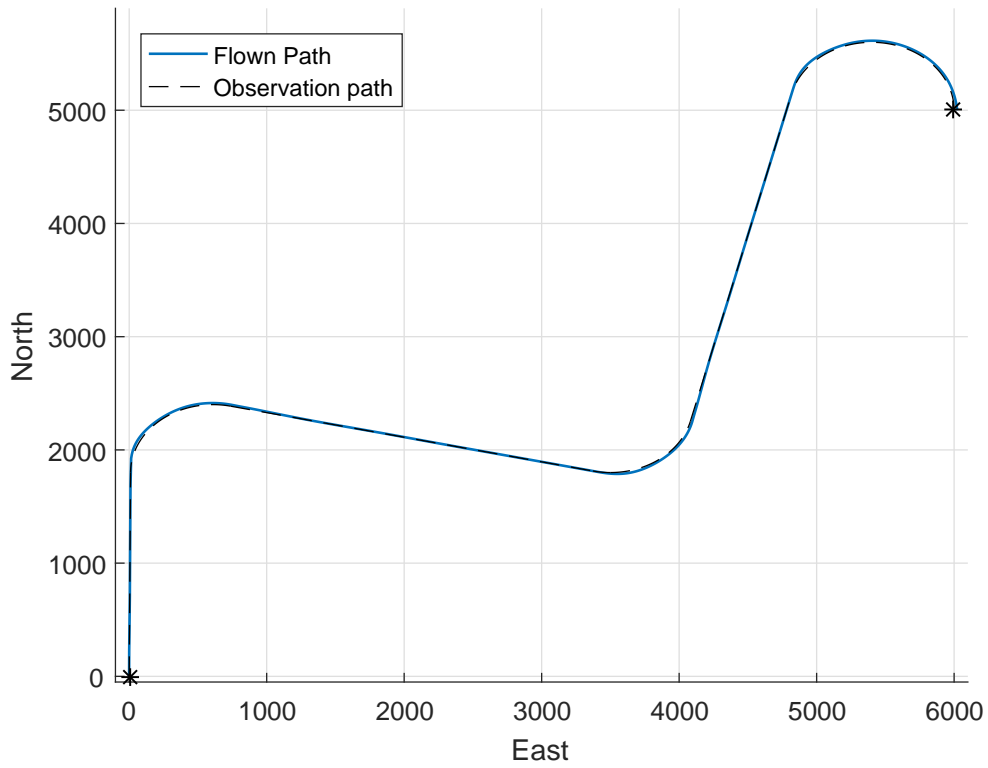


Figure 19: The path flown by the aircraft on the first run.

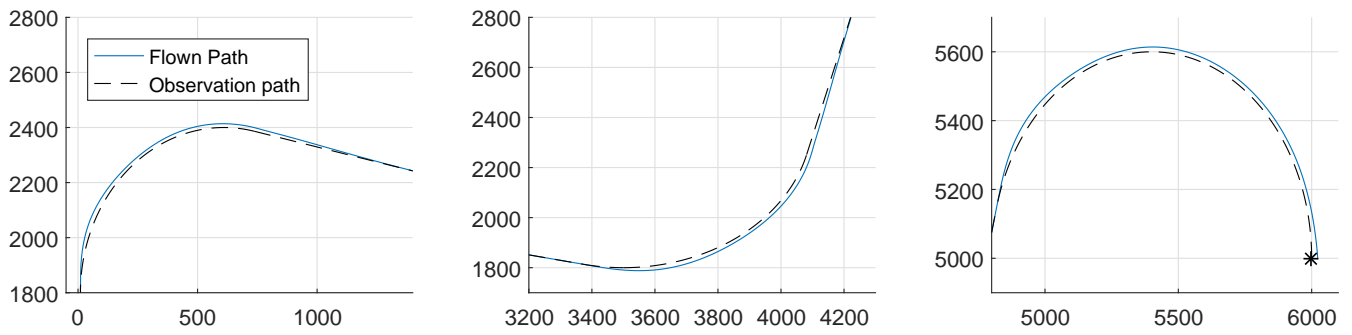


Figure 20: The path the aircraft took through the turns on the first run.

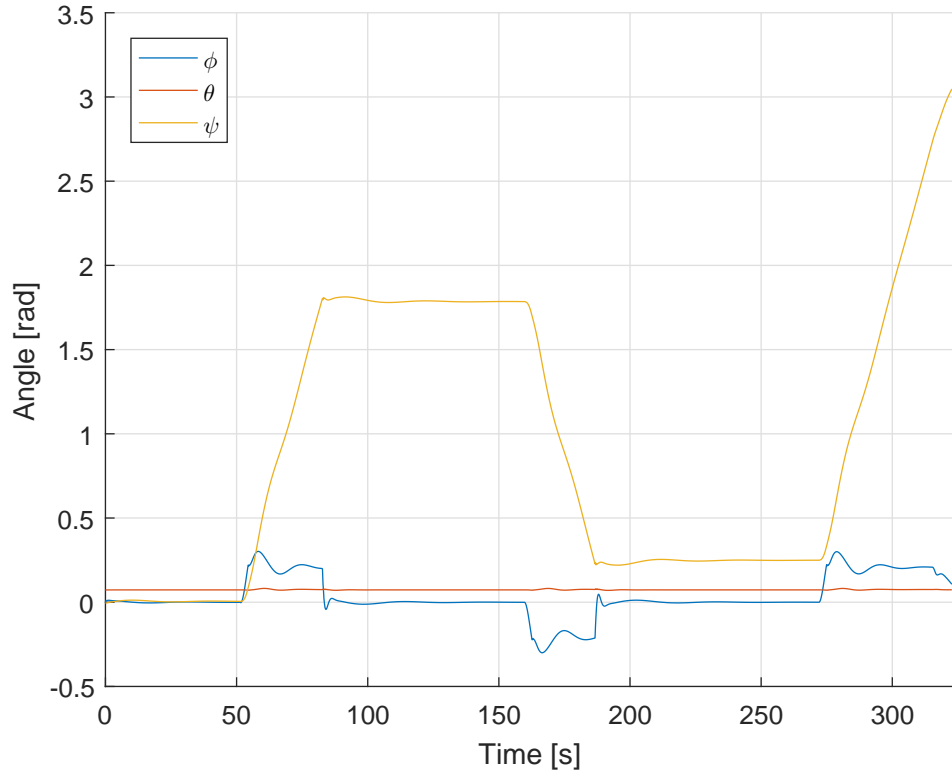


Figure 21: The attitude states of the aircraft during the first run.

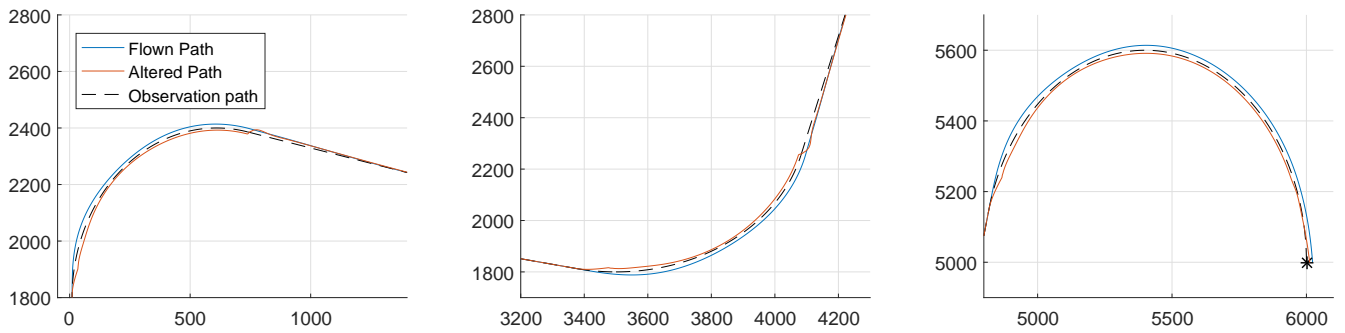


Figure 22: The figure shows how the altered path is compared to the flown path. Only the turns are shown as they are matching during the straight levelled sections.

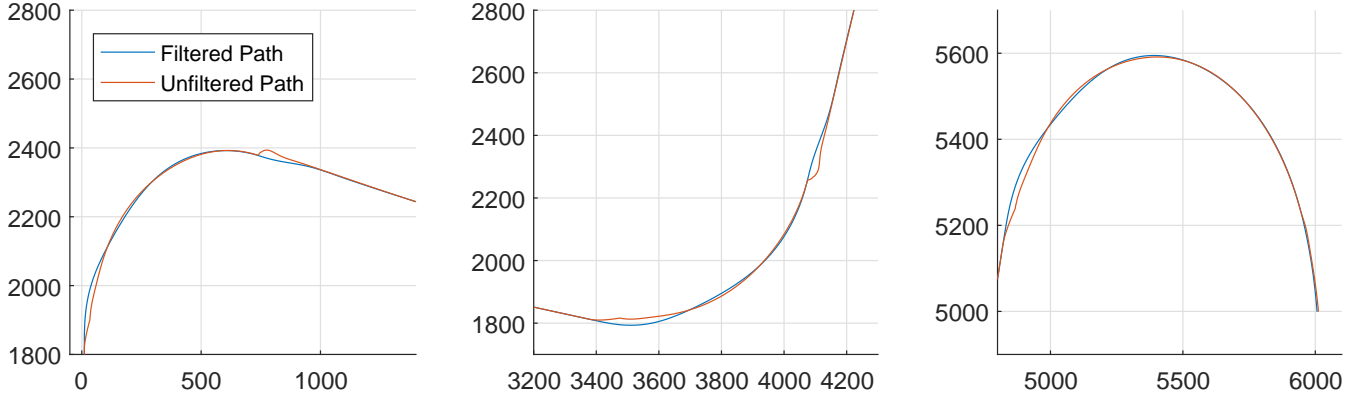


Figure 23: The path created by using the filtered signal for  $\phi$  compared to using the unfiltered.

The result of the simulation when following the altered path is shown in figures (24), (25) and (26). It can be seen that instead of taking the outer path during turns, the aircraft now takes the inner turn which is what we want. It can be seen that  $\phi$  is still uneven during turns, and about the same value as during the first run.

### 8.3 Result: Camera Footprint

The camera footprint for the original path is shown in figures 27 and 28. While the camera footprint is positioned fairly straight above the observation path, the observation path is outside of the camera footprint during turns. The footprint drifts completely off the observation path in the beginning of the turn, but it catches up after the initial "NUDGE". This matches the results from the previous section where the roll  $\phi$  was the highest in the beginning of the turn. There is also a big change in  $\phi$  at the end of the turn, which leads to a large movement of the camera footprint.

For the altered path the camera footprint covers the observation path for the entire path as seen in figures 29 and 30. However, the observation path is not in the middle of the footprint during turns, during turns the camera footprint may drift so the observation path is only visible on the edge of the footprint.

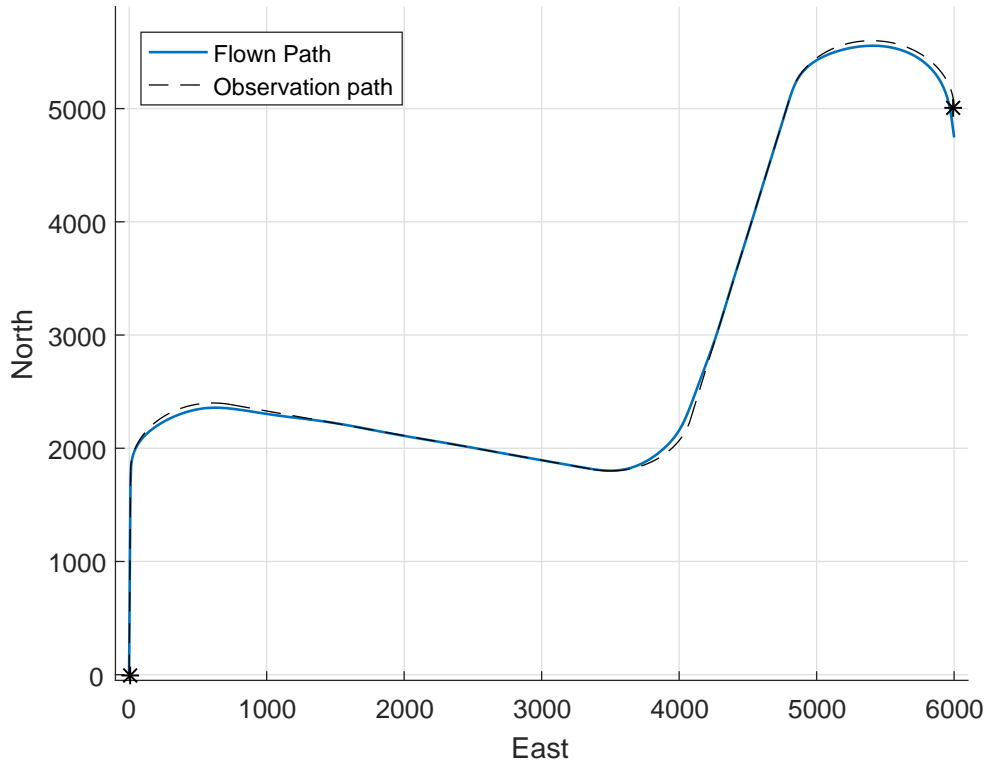


Figure 24: The path flown by the aircraft when following the altered path.

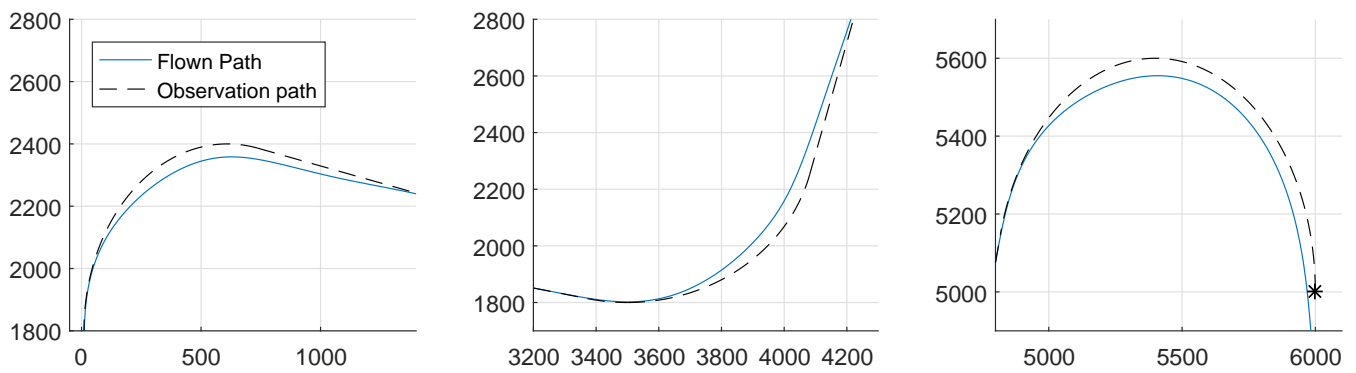


Figure 25: The path the aircraft took through the turns when following the altered path.

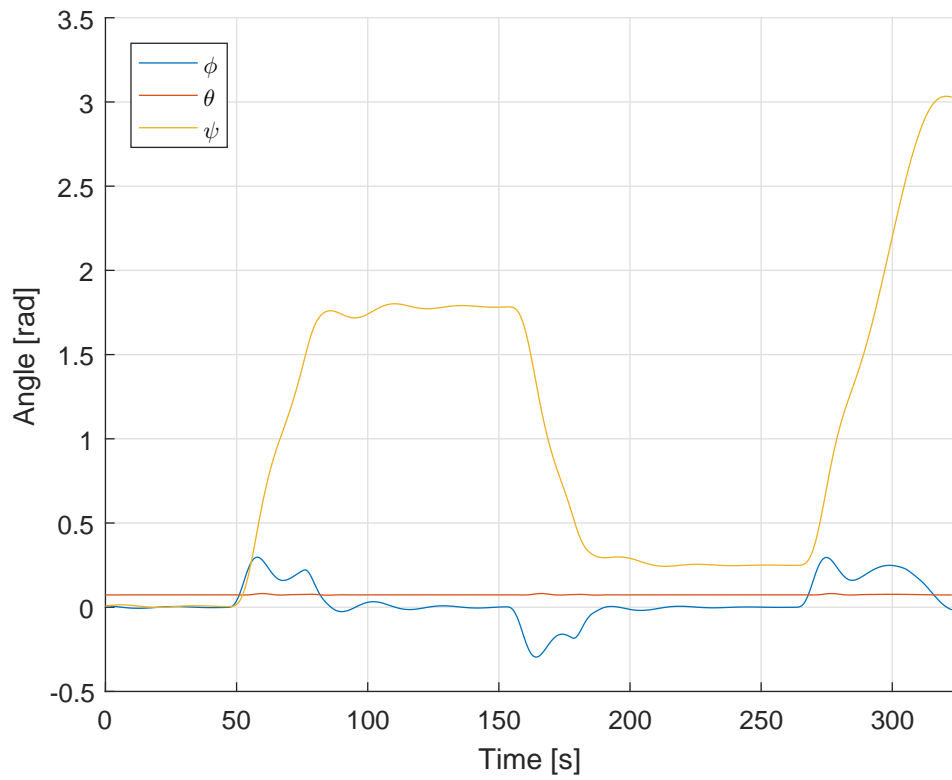


Figure 26: The attitude states of the aircraft when following the altered path.

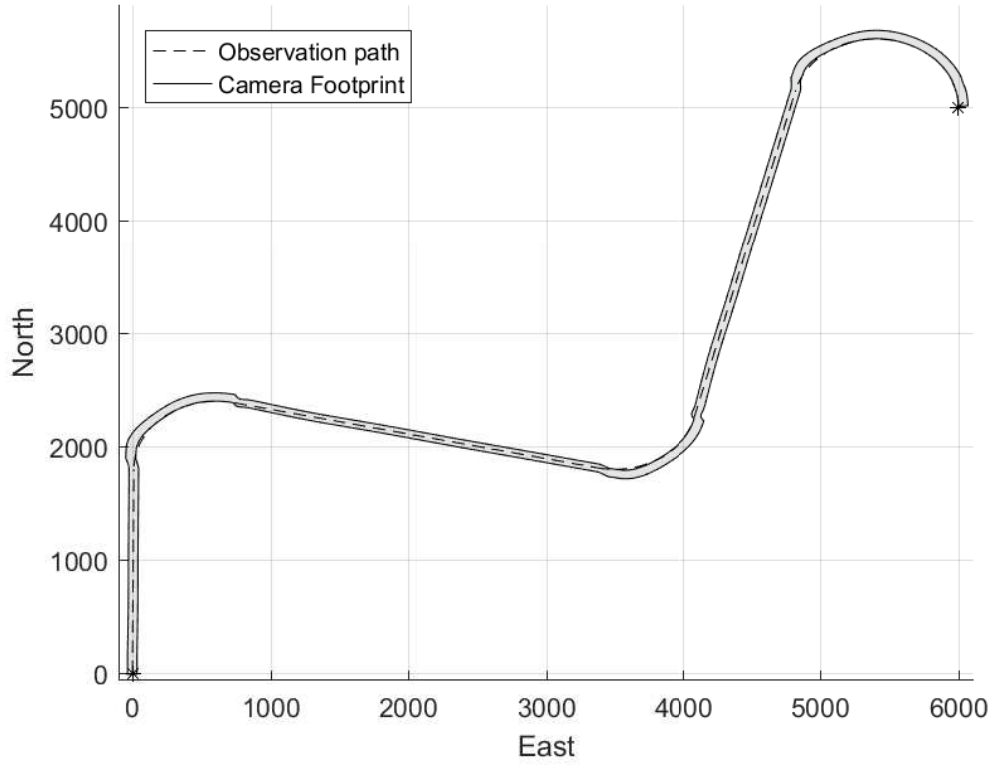


Figure 27: The camera footprint during simulation of the first path.

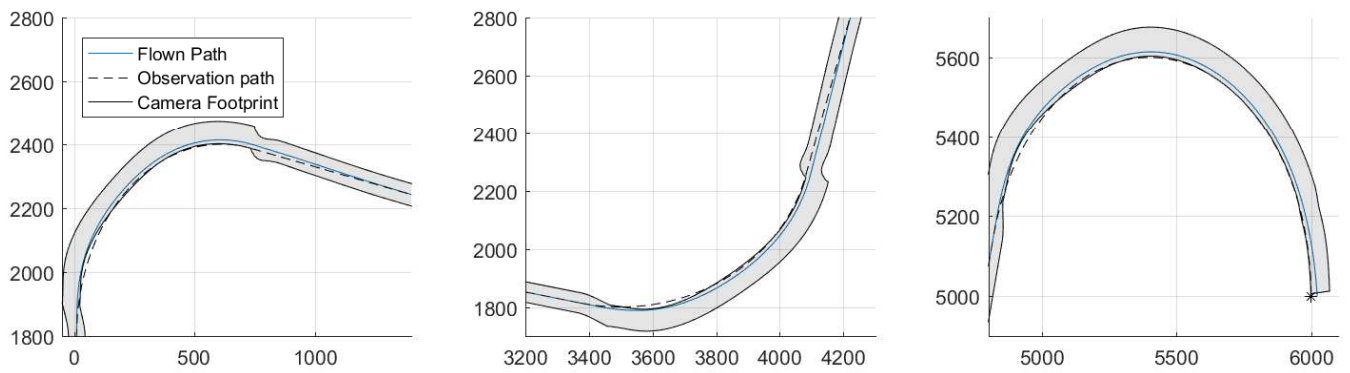


Figure 28: The camera footprint in turns during the simulation of the first path.



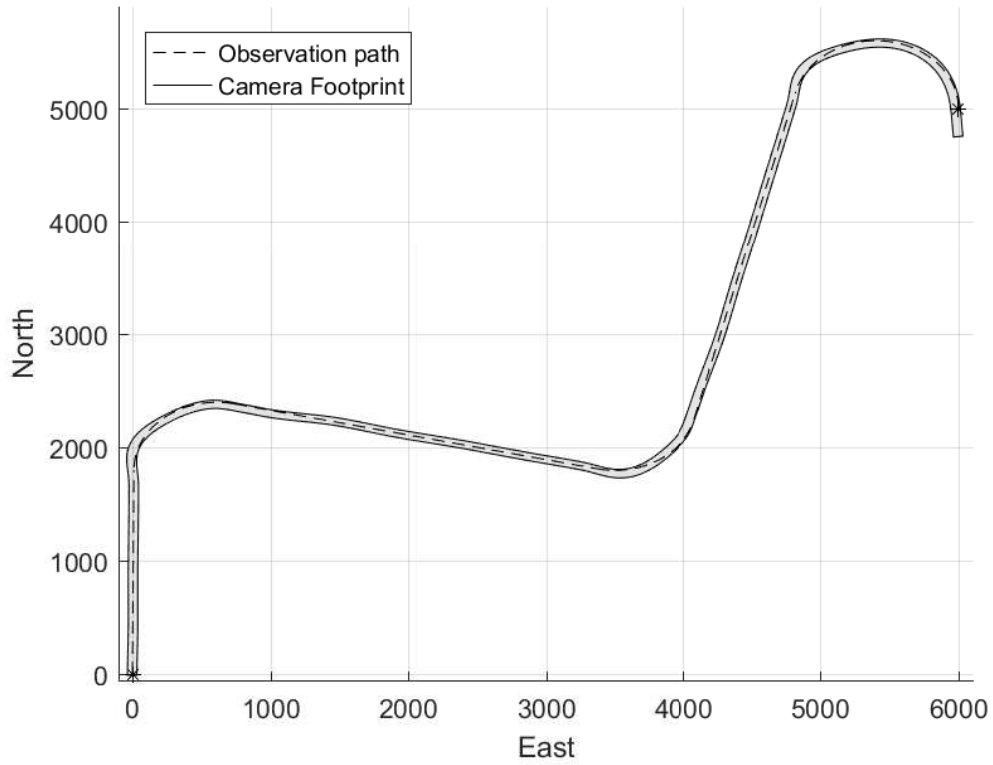


Figure 29: The camera footprint during simulation of the altered path.

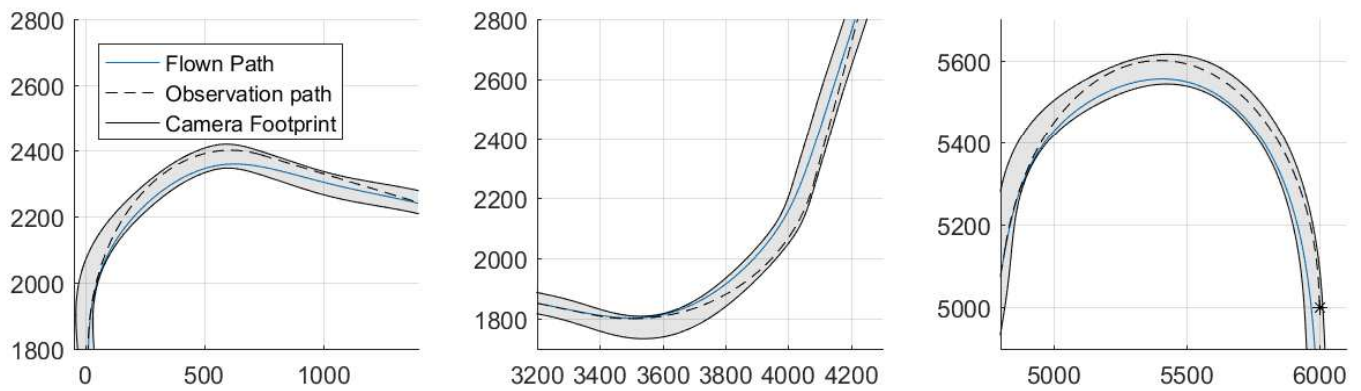


Figure 30: The camera footprint in turns during the simulation of the altered path.

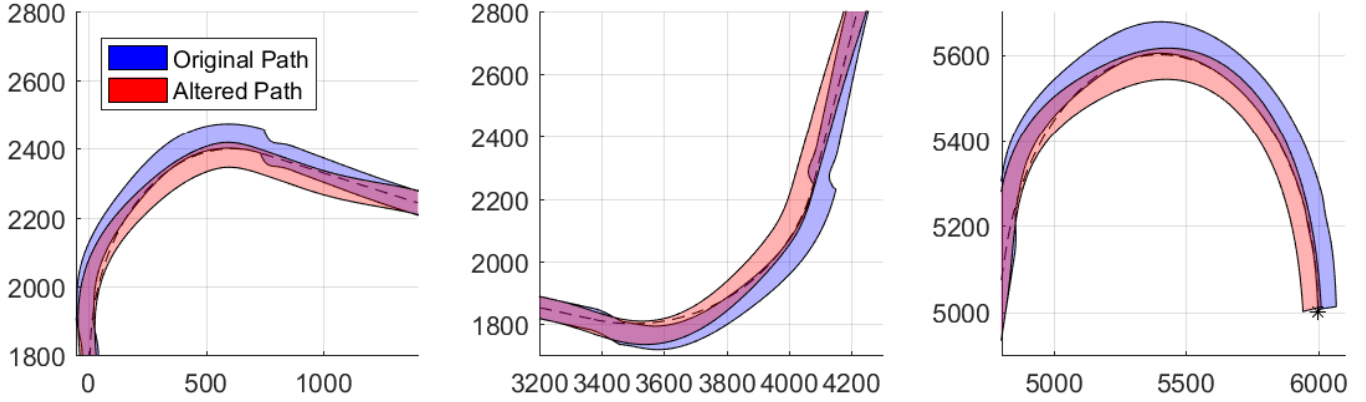


Figure 31: The camera footprint in turns during the simulation of the altered path.

When the two paths are compared in figure 31 the biggest difference is that when following the original path the camera takes the outer turn, and when following the altered path it takes the inner turn. The figures also show that the altered path is smoother than the original. At the end of the two first turns for the original path the aircraft levels the wings quickly, as can be seen in figure 21, which leads to a sideways shift in the camera footprint.

## 8.4 Discussion

The results of the simulation shows that the altered path does a better job observing the ground path than when trying to track the observation path. Tracking the ground path which in this case is to be observed leads to loss of information, which clearly is not acceptable in this type of mission. Another problem encountered in these simulations when tracking the observation path is rapid sideways shifts caused by a rapid change in the roll. The change between images taken during these sections is big, which most likely makes it very difficult to make good use of these images, even though the observation path has been covered. The reason for these rapid changes in roll is because of how the Dubins path is followed. The UAV switches from following a straight path with a fairly constant course, and then switches to follow a circular orbit in a short mo-

ment. This causes a jump in the desired course which again causes a rapid roll. This can most likely be minimized by using a different tuning of the course controller in the autopilot, but is one of the shortcomings by tracking a Dubins path this way (Fossen [19], ch. 10.3.1).

There are also some shortcomings with the altered path used in this simulation. Even though it covered the observation path at all times, the observation path was not centered in the camera footprint. At some points during the flight, and especially in the beginning of the turns, the observation path is so close to the edge of the camera footprint that a small change in roll will most likely cause the camera to lose the ground track. One of the reasons this happens is the strategy used to alter the path. Since the path is only altered when there was roll present in the original flight path, the altered path will not start the turn any earlier than the original path did. Because the altered path cuts the corners of the original path but starts the turn at the same time, the turns of the altered path will be sharper than for the original, thus requiring a higher degree of roll. This is somewhat minimized by using a line-of-sight path follower that tracks the path ahead of the UAV, but the results show that this is not enough.

## **9 Conclusion**

### **9.1 Future Work**

## References

- [1] Mills, S., Ford, J. J., Mejias, L. (2011) "*Vision Based Control for Fixed Wing UAVs Inspecting Locally Linear Infrastructure using Skid-to-Turn Maneuvers*", Australian Research Centre for Aerospace Automation (ARCAA), Queensland University of Technology, Australia
- [2] Fisher, Thomas M. (2016) "*Rudder Augmented Trajectory Correction for Unmanned Aerial Vehicles to Decrease Lateral Image Errors of Fixed Camera Payloads*", All Graduate Theses and Dissertations, Paper 4751, USA
- [3] Ahsan, M., Rafique, H., Abbas, Z. (2012) "*Heading Control of a Fixed Wing UAV Using Alternate Control Surfaces*", National University of Sciences and Technology, Islamabad, Pakistan
- [4] Egbert, J., Beard, R. W. (2007) "*Low Altitude Road Following Constraints Using Strap-down EO Cameras on Miniature Air Vehicles*", Proceedings of the 2007 American Control Conference, New York City, USA (IEEE)
- [5] Beard, R. W., McLain, T. W. (2012) "*Small Unmanned Aircraft: Theory and Practice*", Princeton University Press, United Kingdom
- [6] Dubins, L. E (1957) "*On curves of minimal length with a constraint on average curvature, and with prescribed initial and terminal positions and tangents*", American Journal of Mathematics, vol. 79, no. 3, pp. 497-516
- [7] Owen, M., Beard, R. W., McLain, T. W. (2014) "*Implementing Dubins Airplane Paths on Fixed-wing UAVs*", Handbook of Unmanned Aerial Vehicles, ed. Kimon P. Valavanis, George J. Vachtsevanos, Springer Verlag, Section XII, Chapter 68, p. 1677-1702
- [8] Lugo-Cárdenas, I., Flores, G., Salazar, S., Lozano, R. (2014) "*Dubins Path Generation for a Fixed Wing UAV*", International Conference on Unmanned Aircraft Systems (ICUAS), Orlando, USA

- [9] Yokoyama, N., Ochi, Y. (2009) "*Path Planning Algorithms for Skid-to-Turn Unmanned Aerial Vehicles*", Journal of Guidance, Control, and Dynamics, Vol. 32, No. 5
- [10] Smith, Randall B. (2012) "*Introduction to Hyperspectral Imaging*", MicroImages, Inc.
- [11] Näsi, R., Honkavaara, E., Lyytikäinen-Saarenmaa, P., Blomqvist, M., Litkey, P., Hakala, T., Viljanen, N., Kantola, T., Tanhuanpää, T., Holopainen, M. (2015) "*Using UAV-Based Photogrammetry and Hyperspectral Imaging for Mapping Bark Beetle Damage at Tree-Level*", Remote Sensing (2015), 7, 15467-15493
- [12] Zarco-Tejada, P. J., González-Dugo, V., Berni, J. A. J. (2012) "*Fluorescence, temperature and narrow-band indices acquired from a UAV platform for water stress detection using a micro-hyperspectral imager and a thermal camera*", Remote Sensing of Environment 117 (2012), 322-337
- [13] Suomalainen, J., Anders, N., Iqbal, S., Roerink, G., Franke, J., Wenting, P., Hünninger, D., Bartholomeus, H., Becker, R., Kooistra, L. (2014) "*A Lightweight Hyperspectral Mapping System and Photogrammetric Processing Chain for Unmanned Aerial Vehicles*", Remote Sensing (2014), 6, 11013-11030
- [14] Yong, C., Barth, E. J. (2006) "*Real-time Dynamic Path Planning for Dubins' Nonholonomic Robot*", Proceedings of the 45th IEEE Conference on Decision & Control, San Diego, CA, USA, December 13-15
- [15] Gryte, K., Fossen, T. I. (2015) "*High Angle of Attack Landing of an Unmanned Aerial Vehicle*", Norges Teknisk-Naturvitenskapelige Universitet, 2015
- [16] Lelong, C. C. D., Burger, P., Jubelin, G., Roux, B., Labbé, S., Baret, F. (2008) "*Assessment of Unmanned Aerial Vehicles Imagery for Quantitative Monitoring of Wheat Crop in Small Plots*", Sensors 2008, 8, 3557-3585
- [17] Ramirez-Paredes, J., Lary, D. J., Gans, N. R. (2015) "*Low-altitude Terrestrial Spectroscopy from a Pushbroom Sensor*", Journal of Field Robotics 33(6), 837-852 (2016), Wiley Periodicals, Inc.

- 
- [18] Asmat, A., Milton, E. J., Atkinson, P. M. (2011) "*Empirical correction of multiple flightline hyperspectral aerial image mosaics*", Remote Sensing of Environment 115 (2011), 2664-
- [19] Fossen, Thor I. (2011) "*Handbook of Marine Craft Hydrodynamics and Motion Control*", John Wiley & Sons, Ltd.
- [20] Balchen, J. G., Andreassen, T., Foss, B. A. (2003) *Reguleringsteknikk*, Institutt for Teknisk Kybernetikk, NTNU, Trondheim